Development of an Aggressive Offset Diffuser Testbed with Adaptive Design Characteristics

Zachary T. Stratton[1] and John T. Spyropoulos[2]
Naval Air Warfare Center, Aircraft Division, Patuxent River, MD, USA
Mory Mani[3]
MIT, Cambridge, MA, USA
James Mace[4], Samuel Li[5], Joshua W. Fletcher[6], Bojan Vukasinovic[7], and Ari Glezer[8]
Woodruff School of Mechanical Engineering, Georgia Institute of Technology
Atlanta, GA 30332-0405

A novel approach to the design process of highly compact, reconfigurable aircraft inlet systems beyond established design guidelines will employ active flow control (AFC) and computation adaptive design methodologies in which AFC is an integral part of the design stage. This approach is based on a reconfigurable surrogate diffuser design testbed integrated with AFC coupled with numerical simulation design tools that will enable rapid variations of desired design characteristics. While the new testbed facilitates broad variations of the inlet aspect ratio (AR), bend angle (θ), and curvature, initial investigations focused on characterization of the evolution of the internal flow and its sensitivity to alterations of the base configuration at $AR = 4$ and $\theta = 20°$, 40°, and 60°. Validation of the numerical approach using measured distributions of streamwise surface pressure and total pressure at the aerodynamic interface plane (AIP) yielded an excellent agreement between the experiments and simulations. At inlet $AR = 4$ and bend radius $0.5D_{AIP}$ and aside from secondary corner vortices that intensified past the inner bend no separation was detected past the bend at all θ. At $M_{AIP} = 0.5$, these secondary flow structures resulted in total pressure loss of 2.5% and 0.03 circumferential average distortion.

Nomenclature

AIP = Aerodynamic interface plane

AR = Inlet/channel aspect ratio

D_{AIP} = AIP diameter

DPCP = Circumferential distortion descriptor

[1] Aerospace Engineer, NAWCAD, AIAA Member
[2] Aerospace Engineer - Lead for Inlets, Nozzles, and Aeroacoustics, NAWCAD, AIAA Associate Fellow
[3] Consultant, AIAA Member
[4] Consultant, AIAA Member
[5] Graduate Research Assistant, AIAA Member
[6] Graduate Research Assistant, AIAA Member
[7] Senior Research Engineer, AIAA Member
[8] Professor, AIAA Fellow

L = throat-to-AIP length

r = Radius of curvature at the bend

M = Mach number

TKE = Turbulent kinetic energy

θ = Bend turning angle

ω = Vorticity

I. Introduction

Over recent decades, there have been significant changes in designs and technologies of inlet systems for military aircraft, such as the introduction of compact subsonic diffusers with significant offset and wave rider inlet apertures for supersonic aircraft. These flight platforms have underscored the increasing need to design more compact, offset inlet systems to enable inlet/airframe integration with the forebody or wings of advanced aircraft concepts. However, the realization of such compact inlet systems, having complex inlet apertures and highly offset or serpentine-shaped diffusers, poses significant flow management challenges arising from several sources such as intense streamwise vortices from inlet cowl lips, secondary flows coupled with separation at diffuser turns, and possible embedded transonic shock waves at the inlet throat. Without appropriate flow management techniques, these secondary flow effects can lead to significant pressure losses and distortion at the aerodynamic interface plane (AIP), where the inlet connects to downstream turbomachinery. Altogether, these flow features pose severe challenges to turbine-engine operability and the aeromechanical response of fan blades that can compromise the engine-compression system.

Several investigations since the 1990s have pointed to the potential of passive and active flow control technologies to mitigate the adverse effects of integrated inlet flow on propulsion system performance. Passive vortex generators have been employed with varying success for improving recovery and distortion by affecting the formation and evolution of secondary flow vortices (e.g., vortex breaker fence, Hall et al., 1993), and partial suppression of internal separation (e.g., Anderson and Gibb, 1993, Owens et al., 2008, and Tanguy et al., 2017). Active flow control (AFC) has also been used to improve diffuser performance with less drag penalty than passive vortex generators. Scribben et al. (2006) used microjets in a serpentine diffuser, operating at an inlet Mach number of 0.55, to reduce circumferential distortion by 70%, while improving pressure recovery by 2%, with a jet mass flow rate coefficient C_q of 1%. Anderson et al. (2004) numerically investigated microjets' effect in a redesigned M2129 inlet s-duct and, after a DOE optimization study, were able to reduce DC60 to below 0.1 with a $C_q = 0.5\%$ at a throat Mach number $M_t = 0.7$. Gartner and Amitay (2015) utilized a variety of AFC devices, including pulsed jets, sweeping jets, and a blowing slot, to improve total-pressure recovery in a rectangular diffuser. The slot was less effective than the sweeping and pulsed jet arrays, even when used with higher C_q. Rabe (2003) tested microjets in a double-offset diffuser attached to a bell-mouth inlet, with the bulk flow fluidically driven by a gas-turbine engine and mass injection driven by bleed from that engine. With a bleed rate of 1% ($M_t = 0.55$) at the cruise condition, circumferential distortion was reduced by more than 60%. Harrison et al. (2013) simulated, and experimentally verified the favorable superposition of ejector-pump-like suction and blowing for a thick-boundary-layer ingesting serpentine diffuser at $M = 0.85$ in the freestream. They found a 50% reduction in DC60 from using a circumferential blowing scheme, which could be increased to 75% by adding suction. Garnier

(2015) performed a spectral analysis of the effectiveness of pulsed and continuous blowing to reattach flow at $M_{AIP} = 0.2$ to 0.4 in an aggressive s-duct using an array of dynamic-pressure sensors. It was found that pulsed blowing effects dynamic-distortion fluctuations at the forcing frequency, but they could match the performance of continuous jets at half the C_q. In addition to conventional jets, synthetic jets have been tested in internal flows for their effectiveness in improving performance. Amitay et al. (2002) investigated separation control in a non-diffusing serpentine duct using an array of synthetic jets and were able to reattach flow up to $M = 0.2$ completely. Mathis et al. (2008) also utilized synthetic jets to reattach flow at $Re = 4.1 \cdot 10^4$ along a high curvature region of an s-duct diffuser and verified flow reattachment with particle image velocimetry (PIV). Gissen et al. (2014) utilized a combination of vanes and synthetic jets to achieve a 35% reduction in circumferential distortion in a BLI offset diffuser operating at $M_{AIP} = 0.55$. Burrows et al. (2019) modified the mold-line of an offset diffuser to trap vorticity concentrations. They utilized fluidic-oscillating jets to control the vorticity and ultimately reduce engine-face distortion by 68% with a C_q of 0.25%. Burrows et al. (2021) showed that a significant source of the total pressure distortion was caused by a local flow separation downstream from the second bend of their serpentine diffuser and demonstrated that active flow control reduced the mean circumferential distortion by 60% with C_q of about 0.5%. Following the addition of a cowl inlet to the diffuser, Burrows et al. (2024) reported the formation of a system of strong inlet streamwise vortices along with a sharp rise in total pressure losses. Therefore, the primary flow control task changed from reduction of distortion to total pressure recovery and the authors used aerodynamic bleed through the cowl to mitigate these losses.

While these earlier investigations clearly demonstrated the significant potential of active flow control for managing the complex flows within integrated inlet systems, AFC was typically considered and applied to inlet designs *a posteriori*, for ad-hoc performance improvements. Because such AFC implementations have been significantly constrained by existing hardware configurations, their effects on the flow and efficiency were limited.

The overarching objective of the current effort is to demonstrate the utility of incorporating AFC technologies from the inception of the diffuser's design. This is accomplished using a reconfigurable surrogate diffuser design testbed integrated with AFC and coupled with numerical simulation design tools that will enable adaptive, rapid variations of desired design characteristics. To this end, the conceptual system shown in Figures 1 and 2 will enable rapid exploration of diffuser designs having desired characteristics (e.g., area ratio, length, degree of offset, aperture aspect ratio, etc.) in which performance shortcomings associated with the internal flow will be overcome by coupled iterations of the diffuser geometry and integrated AFC using validated numerical design tools. In the present experimental-numerical effort experimental data is obtained to verify the accuracy and overcome shortcomings of CFD for full validation. The test facility and modular experimental testbed that enables quick changes in test configurations (aspect ratio, bend angle, and bend radius) is described in §II, the numerical setup and methods are discussed in §III, calibration of the mass flow rate to the inlet's bellmouth section relative to measurements at the AIP is described in §IV, the experimental and numerical data are compared in §V, and the flow field obtained from the numerical simulations within the facility is analyzed in §VI.

II. Experimental Setup and Flow Diagnostics

The present experiments are performed in the Georgia Tech open-return, pull-down, subsonic wind tunnel driven by a 150 hp blower, as shown schematically in Figure 1 along with the diffuser

model. The total pressure distribution at the AIP is measured using a 40-probe total pressure rake within a cylindrical conduit having diameter D_{AIP} = 12.7 cm. Downstream of the total pressure rake section, the flow is expanded through a tunnel diffuser and a 90-degree turn into the system's blower, controlled remotely by a variable frequency drive. The blower's outlet is connected to a flow silencer to reduce noise, and a water-cooled low-pressure drop heat exchanger (not shown) that is cooled by a dedicated chiller controls the return air within 1-2° C.

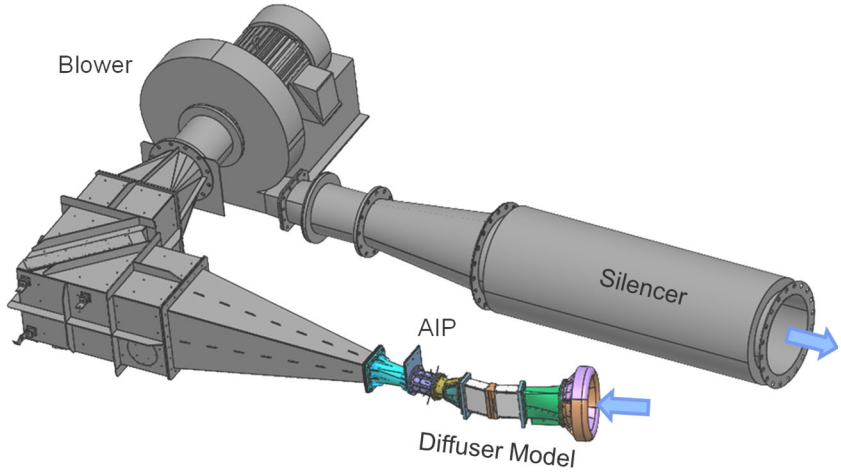

Figure 1. *CAD model of pull-down wind tunnel facility having the diffuser model at its intake.*

The modular diffuser testbed model shown in Figures 1 and 2, can be constructed from interchangeable mating elements to yield independent variations of aspect ratio, bend turning angle, and turning radius. Ambient air is drawn through a bellmouth section having an inlet diameter 3.9D_{AIP}, followed by a circular to rectangular transition section to the inlet of a transparent constant cross section channel upstream of an interchangeable bend section where bends of different angles and turning radii can be installed. The flow duct downstream of the bend is another transparent constant area channel that connects the bend to a rectangular-to-round diffuser adapter into the AIP. The constant cross section ducts are designed to enable optical measurements using particle image velocimetry (PIV), and the downstream duct can be removed so that the bend is connected directly to the downstream diffuser. In the present investigation, the aspect ratio of the modular diffuser is $AR = 4$, and the bend's inner radius is $r = 0.5\ D_{AIP}$ while bend angles $\theta = 20°$, 40°, and 60° are tested over a range of AIP Mach numbers $0.1 < M_{AIP} < 0.54$. It should be noted that while the model bends are in the horizontal plane, the experimental and numerical data are presented for bends in the vertical plane as oriented in Figure 2.

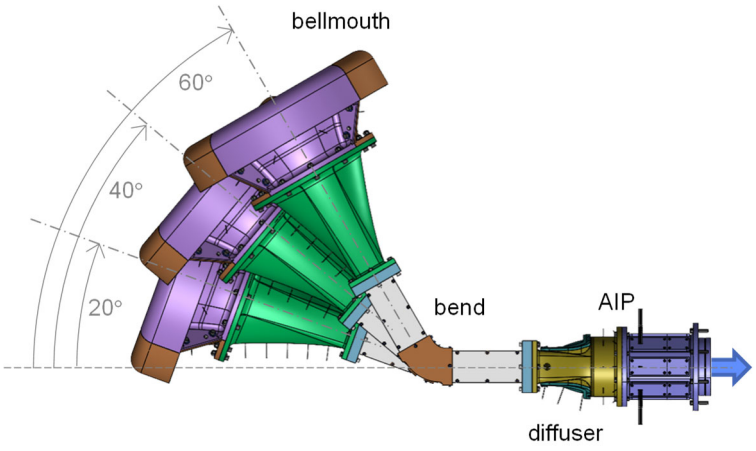

Figure 2. *Overlaid CAD images of the modular diffuser model with bends at $\theta = 20°, 40°$, and 60°.*

The 40-probe total-pressure rake at the AIP is constructed from eight radial arrays each of five total pressure tubes at r/R = 0.27, 0.38, 0.51, 0.67, and 0.9 that are azimuthally spaced 45° apart around the circumference of the AIP. The total pressure rake is supplemented with a matching

array of eight static pressure ports that are each located on the diffuser wall 0.4D upstream of the AIP. The total and static pressure measurements are used to compute the AIP Mach number, mass flow rate, total-pressure recovery, as well as flow distortion descriptors per SAE ARP1420b (2011). The mass flow rate is normalized with respect to standard sea level pressure and temperature conditions. Additional static pressure ports are distributed along the centerlines of the side and bottom walls of the bellmouth and diffuser sections, and the inner and outer surfaces of the bend. An azimuthal array of equally-spaced eight static pressure ports over the aft end of the bellmouth are used for monitoring the mass flow rate through the model following the calibration discussed in §IV.

The static and total pressures are measured using a PSI Netscanner system where each set of pressure measurements is averaged over 64 independent samples, while the time-averaged static and total pressures are computed from fifty such sets. The manufacturer specified accuracy of each scanner channel is ±17.25 Pa and the overall uncertainty of the time-averaged pressure is less than 1%. The static pressure around the circumference of the bellmouth is measured using a 10 torr MKS Baratron transducer sampled (uncertainty of about 1.5 Pa) using a computer-controlled rotary valve.

III. Numerical Setup

Flow Solver and Turbulence Model The CharLES LES code, developed by Cascade Technologies, is used to solve the compressible, time-dependent, filtered Navier-Stokes equations for this diffuser configuration. CharLES utilizes a density-based finite-volume method on unstructured grids, where fluxes are computed with a second-order scheme (Ham et al., 2006). The time integration uses an explicit third-order Runge-Kutta scheme. The mesh generation is handled by Stitch, a tool within the CharLES suite, which is automatic and based on the computation of Voronoi diagrams (Bres et al., 2017). This method results in a smooth mesh of nearly isotropic cells throughout the domain, which is well-suited for LES.

CharLES has implemented a wall-stress-based model that significantly reduces the near-wall grid requirements. This model's equations are based on the algebraic formulation of the one-dimensional equilibrium stress model (Kawai and Larsson, 2010). These equations are solved at each wall-adjacent cell centroid at each time step for wall shear stress, which serves as the Neumann boundary conditions for the momentum equations. This wall model does not account for the inner layer solution's unsteadiness or pressure gradient effects. The static model by Vreman (2004) and the dynamic Smagorinsky model (Germano et al., 1991) are utilized to account for the sub-grid-scale stresses.

Computational Domain and Simulation Details The computational domain used for the diffuser in this study is shown in Figure 3 and is based on the CAD model of the GT facility and test model hardware. It extends the bellmouth (shown in yellow) to incorporate a sizeable hemispherical inlet region. The rakes are included in the rake housing. A total pressure boundary condition is applied to the inflow surface, set at standard atmospheric day conditions. The tunnel walls through the rake housing, are set as no-slip walls where the algebraic equilibrium wall model is applied. The extensions, downstream of the AIP rake housing, are set as free-slip walls. The outlet is a pressure boundary condition, where the pressure is set to achieve a desired mass flow rate; this flow rate will determine the Mach number at the throat.. Simulations were conducted at an $M_{AIP} = 0.4$ at $\theta = 20^o$, 40^o, and 60^o. Additionally, three separate simulations were completed at $M_{AIP} = 0.25$,

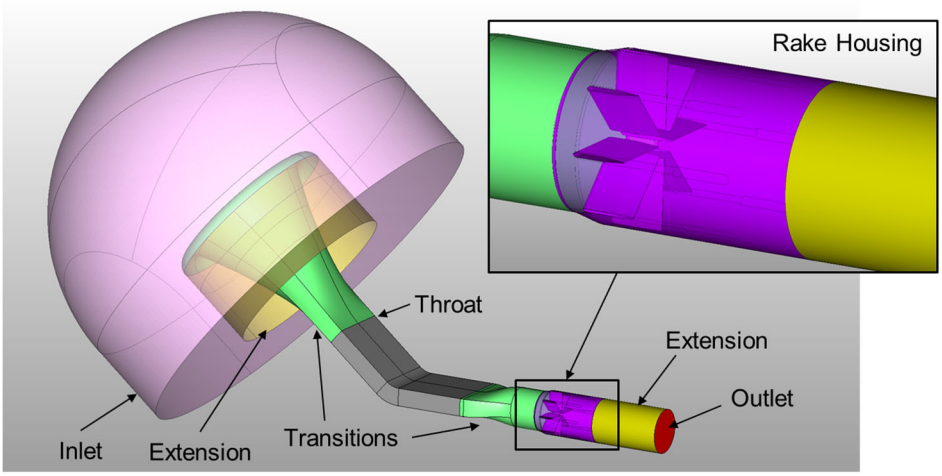

Figure 3. *Computational Domain.*

0.4, and 0.6 for the calibration configuration, which connects the circular bellmouth directly to the circular AIP; this will be discussed in Section IV. To better understand the rake impact on the pressure measurements, two calibration configurations were considered, one without the rake housing and one that included the rake housing.

The grids used in this study are summarized in Table 1, the cell count is the total number of elements in the computational domain, and average y^+ is measured at the gray walls, between the transitions, shown in Figure 3. A grid sensitivity study was conducted for $\theta = 20^o$ at $M_{AIP} = 0.4$. Table 1 highlights the accuracy compared to the experimentally measured mean pressure recovery and mean distortion at the AIP. Cross-sectional cuts at the AIP, shown in Figure 4, highlight the regions in which the grids were varied. The accuracy of the mean pressure recovery for each grid was found to be consistent, however, $DPCP_{avg}$ was found to vary. Refining the near wall region in M2 had little impact on this quantity and negligible impact on flow structure, as shown in Section V. Off-wall refinement was added in M3 to capture better large-scale vorticity originating at the bend; however, this, too, had a negligible impact. Therefore M1, shown in Figure 4b, was considered to provide a grid-converged solution for this simulation and is used for all subsequent simulations in this study. A subsequent study investigating the sub-grid scale model impacts found that the dynamic Smagorinsky model improved the $DPCP_{avg}$ prediction to within 2% of the experimentally measured value. Therefore, this model is used throughout this study.

Table 1. *Mesh details and accuracy compared with experimental measurements using Vreman SGS model.*

Mesh	Cell Count (1e6)	y^+_{avg}	p_o/p_a Accuracy (%)	$DPCP_{avg}$ Accuracy (%)
M0	150	44	0.2	26.1
M1	320	22	0.2	8.9
M2	730	11	0.2	10.7
M3	480	22	0.2	9.1

All simulations were run on the U.S. Department of Defense Narwhal and Raider clusters using GPU resources. Using 40 A100 GPUs, M1 completes 40 characteristic diffuser-flow-convection times utilizing the distance between the throat and AIP in 24 hours.

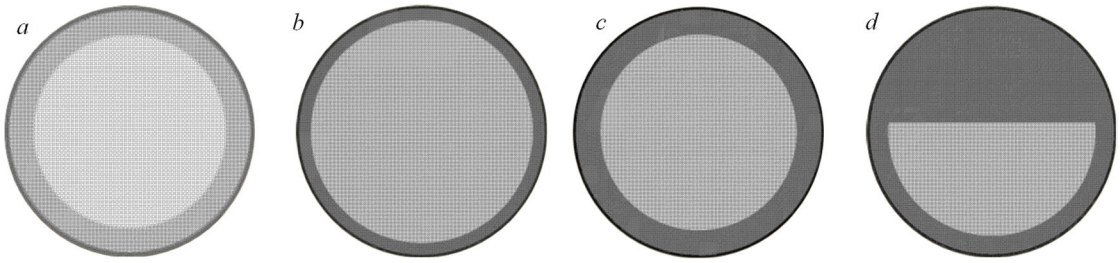

Figure 4. *Grid structure based on Voronoi diagrams for M0 (a), M1 (b), M2 (c), and M3 (d).*

IV. Mass Flow Rate Calibration

Although the total pressure measurements using the 40-probe rake, in combination with the wall static pressures around the AIP circumference, can be used to estimate the total mass flow rate through the test model, the fidelity of such an estimate clearly degrades in the presence of flow separation and secondary flow structures, due to the finite spacings of the AIP total pressure probes. To overcome this issue, a calibration procedure was developed to assess the mass flow rate from measurements of pressure drop through the bellmouth inlet section. For this purpose, the full diffuser model shown in Figure 2 was reduced to a straight model with a circular cross section where the bend, its upstream and downstream rectangular sections, and the downstream transition diffuser were replaced with a conical transition section that connected the bellmouth directly to the AIP (Figure 5). As shown in the cross-sectional view in Figure 5, the bellmouth is equipped with eight surface static pressure ports denoted $p_{B1} - p_{B8}$, that are that are spaced azimuthally 45° apart upstream of the conical transition section. The eight circumferential static pressures are measured individually and averaged to provide a reference bellmouth pressure for calibration of the mass flow rate through the AIP that is estimated from measurements of the 40-probe rake. As noted in §II, each of the eight rakes has a wall static pressure port $0.4D_{AIP}$ upstream from the AIP labeled $p_{C1} - p_{C8}$. The present measurements demonstrated that azimuthal variations of the static pressure measured by the arrays $(p_B)_i$ and $(p_C)_i$ were negligible, with average pressure varying less than 1%.

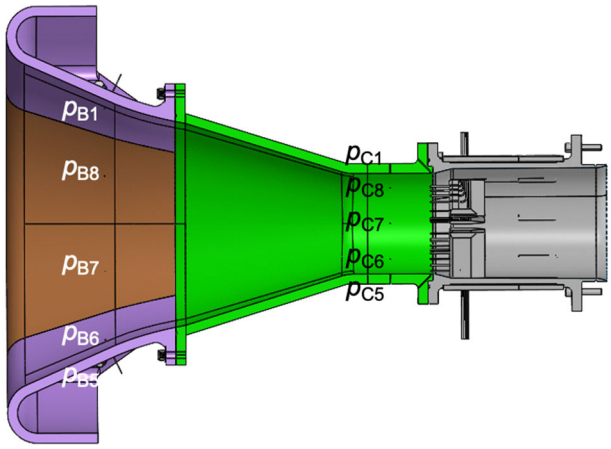

Figure 5. *Mass flow rate calibration model where the bend and diffuser sections were replaced with a conical transition section.*

The calibration procedure was carried up to $M_{AIP} = 0.7$. Figure 6a shows the variation of the AIP Mach number estimated from the 40-probe total pressure measurements using the static pressure array $(p_C)_i$ with the static pressure drop across the bellmouth Δp_B. As shown, for $\Delta p_B < -150$ Pa, M_{AIP} increases nearly linearly with Δp_B. Furthermore, when the numerical setup includes the conical diffuser and AIP pressure rake (Figure 5), three numerical simulations agree very well with M_{AIP} computed from the measurements. Similar to Figure 6a, it was shown that the mass flow rate through the AIP $\dot{m}_c \sim (\Delta p_B)^{0.5}$ and agrees well with the simulations. The variation of $\dot{m}_c$ with M_{AIP}in Figure 6b shows that $\dot{m}$ varies nearly linearly with Δp_B in two domains of its rate of change

that decreases somewhat for $M_{AIP} > 0.45$.

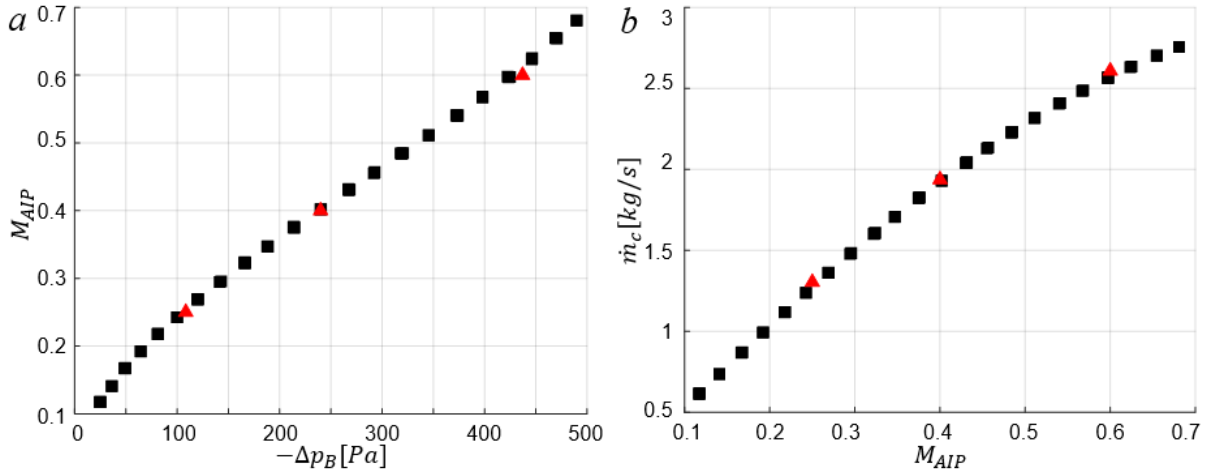

Figure 6. *a) Calibration of the diffuser Mach number at the AIP with the bellmouth pressure drop, and b) Variation of diffuser mass flow rate with M_{AIP} both shown using (■). The corresponding three numerical simulations are also included (▲).*

V. Comparison between Experimental and Numerical Results

Initial insight into the topology of the flow through the test model at the mid-range bend angle $\theta = 40°$ is evident from color raster plots of the total pressure distribution at the AIP, as shown in Figures 7a-c for $M_{AIP} = 0.3$, 0.4, and 0.5, respectively. The distributions exhibit two concentrations of total pressure deficit at the top and bottom of the image that are associated with the flow over the convex (inner) and concave (outer) surfaces of the bend and exhibit radially wider deficit domain at the top is associated with the convex surface of the bend, while the bottom deficit domain remains flat. These features clearly intensify with the Mach number but do not change significantly in structure, signifying the similar flow features through the AIP. It should be noted that the flow topology captured at the AIP is a result of the flow through the bend, the constant cross section rectangular duct downstream, and the expanding surfaces of the diffuser adapter upstream of the AIP. The total pressure deficit in Figure 7c indicates local spanwise separation across the diffuser and potentially at the downstream end of the bend surfaces that can develop Gortler vortices on the concave surface and undergo centrifugal instability on the convex surface. The numerical simulations discussed in connection with Figure 15 reveal the presence of counter-rotating vortex pairs along the top and bottom surfaces of the AIP that are associated with the pressure deficits seen here. It is noted that at $\theta = 40°$ in Figure 7, the increase in M_{AIP} from 0.3 (Figure 7a) to 0.5 (Figure 7c), results in increased total pressure losses from 0.99 to 0.975, while the time-averaged circumferential total pressure distortion $DPCP_{avg}$ increases from 0.01

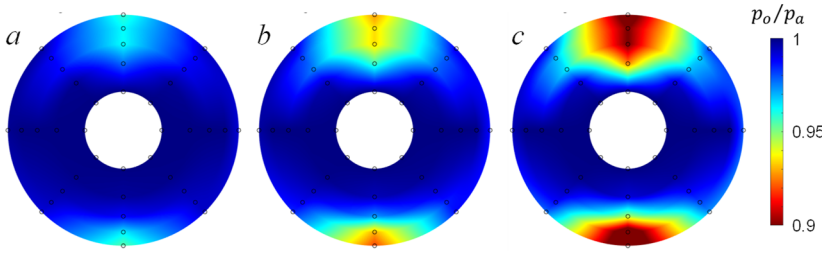

Figure 7. *Raster color plots of the total pressures at the AIP for bend angle $\theta = 40°$ at $M_{AIP} = 0.3$ (a), 0.4(b), and 0.5 (c).*

to 0.03.

Further insight into the structure of the time-averaged flow through the test model is gained from measured distributions of the surface static pressure for the same model configuration ($\theta = 40°$) at $0.1 < M_{AIP} < 0.54$. The pressure distributions are shown in Figure 8 in terms of the variation of the pressure coefficient $C_p = 2 \cdot \left(p/p_{ref} - 1\right)/\left(\kappa \cdot M_{AIP}{}^2\right)$ with axial distance x relative to the AIP, where $\kappa = 1.4$ is the specific heat ratio for air, and the reference pressure $p_{ref} = \overline{p_{C_i}}$. In addition to discrete experimental points the corresponding pressure distribution from the simulations is also shown for $M_{AIP} = 0.4$. For identification of the pressure variations along the diffuser, a CAD model is shown above each plot such that the pressure ports are aligned with the corresponding data. Figure 8a shows the pressure distributions along the bottom surface of the diffuser. The five most-upstream pressure ports are distributed along the round to rectangular contraction section and clearly indicate the flow acceleration. The numerical data indicates that this acceleration continues up to the full transition to the constant cross section rectangular channel. Following a quick recovery at the entrance, the pressure remains reasonably invariant leading into the bend. In the concave outer bend, the flow initially experiences an adverse pressure gradient, followed by acceleration along the outward section of the bend.

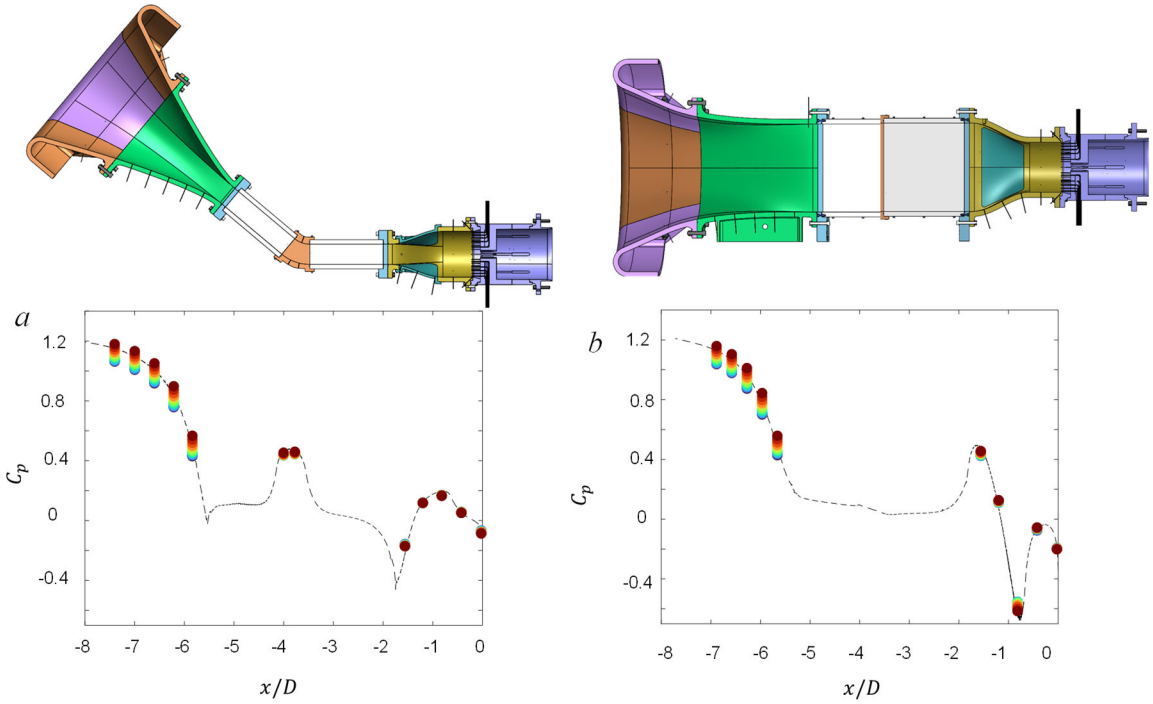

Figure 8. *Measured distributions of surface static pressure along the bottom wall (a) and side wall (b) at $\theta = 40°$ and M_{AIP} = 0.10 (●), 0.14 (●), 0.19 (●), 0.23 (●), 0.27 (●), 0.32 (●), 0.36 (●), 0.39 (●), 0.41 (●), 0.45 (●), 0.50 (●), 0.54 (●). The numerical result (---) are shown for M_{AIP} = 0.4.*

The pressure within the rectangular duct downstream of the bend continues to decrease into the diffusing adapter section to the AIP. However, there is a reversal upon entry into the diffuser, and the change in geometry imposes an adverse pressure gradient. Finally, the pressure indicates an accelerating flow into the AIP past the diffuser. Overall, this pressure distribution along the bottom surface indicates that there are two transitions that possibly can induce flow separation by imposing strong adverse pressure gradients – the upstream section of the bend leading into the wall turning ($-4.2 < x/D < -3.8$) and across the diffusing section ($-1.7 < x/D < -0.8$).

The side wall pressure distributions are shown in Figure 8b. While the upstream acceleration remains similar to that in Figure 8a, as the flow traverses the bend and its upstream and downstream channels, there is only a mild pressure drop before the flow approaches the transition to the AIP. The flow decelerates prior to entering the transition and afterward reverses into acceleration due to the converging geometry of the adapter along this surface. Similar to the geometry change into the adapter, some deceleration is imposed on the flow just upstream from the next geometry change at the exit from the adapter. Finally, upon exiting the adapter, another reversal is seen, and the flow accelerates into the AIP, albeit at a much lower rate. Not surprisingly, this pressure distribution, in contrast to the distribution in Figure 8a, exhibits milder adverse pressure gradients, particularly upstream from the adapter ($-2 < x/D < -1.7$), while the exit from the adapter ($--0.8 < x/D < -0.4$) induces pressure gradient at the similar level as that leading into the bend in Figure 8a.

Following the discussion of the flow at $\theta = 40°$, its evolution at bend angles $\theta = 20°$ and 60° are considered. Measured and simulated color raster plots of the total pressure at the AIP at $M_{AIP} \approx 0.4$ are shown in Figure 9. The experimental results (Figures 9a–c) indicate that, in principle, the topology is similar at all angles, indicating that the underlying flow physics is similar as well, a topic that will be further examined by analysis of the numerical results in the last section. Nonetheless, some secondary trends are observed with an increase in the bend angle. The total pressure contour at the AIP which is aligned with the inner bend surface (at the top) indicates that the most focused pressure deficit is for the lowest bend angle (Figure 9a). As the bend angle increases, it is interesting that almost no change is seen in experimental results of the radial outward spreading of this deficit domain. However, there is a consistent azimuthal spreading of this domain with the increase in θ. The AIP signature of the flow over the outer bend (at the bottom) indicates a very limited outward spreading of the total pressure deficit. As the bend angle is increased, there is a rather subtle "compression" of this zone, such that it becomes pulled closer to the surface and away in the azimuthal direction. While the corresponding full CFD contour plots of the total pressure distribution (Figures 9d–f) uncover a much richer structures at the AIP top and bottom, most of the trends seen in experimental data are observed as well, except

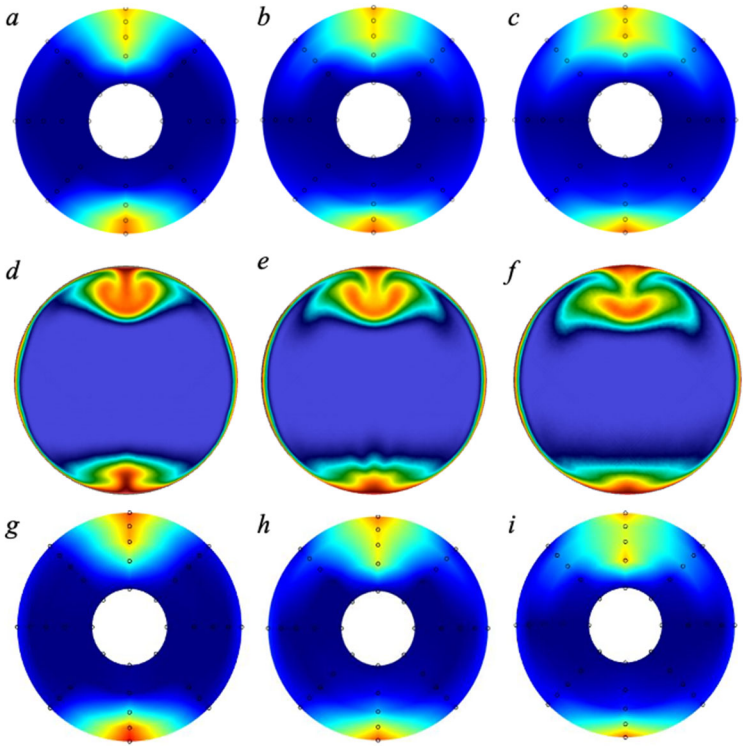

Figure 9. *Color raster plots of distributions of total pressure at the AIP for $\theta = 20°$ (a, d, g), 40° (b, e, h), and 60° (c, f, i): measured by the 40-probe rake (a–c), simulated (d–f), and numerical simulation of the 40-probe rake (g–i) at $M_{AIP} = 0.4$. The color bar is the same as in Figure 7.*

that a better resolution does show some radial outward expansion of the total pressure deficit at the top central region. A mushroom-shaped peak deficit in the top region illustrates how the low momentum fluid near surface is pulled right at the top, and subsequently swirled around, arguably due to the synchronous action of the vortex pair, which is also addressed further in the last section. Similarly, there is a pull of the low momentum fluid away from the surface at the AIP bottom, but absence of the mushroom shape suggests that the vortices acting along the bottom surface are weak and/or spaced away such that there is less synchronous action. Lastly, for direct comparison of these mean flow features, the CFD results shown in Figures 9d–f are numerically subsampled at locations of the experimental 40 probes. The resulting contour plots are shown in Figures 9g–i, plotted in the same way as experimental data, such that each plot directly compares to the experimental plot in Figures 9a–c. Generally, a very good comparison in the total pressure distributions between experiments and simulations is seen in both the topology structure and the deficit magnitudes. Beyond qualitative similarities, this comparison is quantified by examining the AIP flow metrics. For the experimental results shown in Figures 9a–c, recovery decreases from 0.986 to 0.984, to 0.983, with increasing bend angle, while the numerical results are generally higher by between 0.1-0.2% in recovery. As for the circumferential averaged distortion coefficient $DPCP_{avg}$, experimental data indicate an increasing progression from $DPCP_{avg} = 0.0208$ to 0.0181, to 0.0174. This finding might be somewhat counterintuitive, since this distortion coefficient appears to slightly decrease with the increase in the bend angle. The corresponding numerical estimate of the $DPCP_{avg}$ indicates even smaller change with θ, yielding a progression in this descriptor from $DPCP_{avg} = 0.0185$ to 0.0180, to 0.0179.

The flow evolution with changes in the bend angle θ is assessed using surface pressure distributions along the central bottom and side surfaces of the diffuser at $M_{AIP} \approx 0.4$ (Figure 10). As expected, based on the prior comparison for the fixed geometry in connection with Figure 8, Figure 10 indicates that there is an excellent agreement between experimental and numerical results. One notable difference relative to Figure 8 is that since the projections of the pressure ports along the x axis upstream of the bend depend on θ, the upstream pressure distributions fan upward with increasing θ. This is clearly seen in either the bottom (Figure 10a) or side (Figure 11b) distributions. Still, as the flow path downstream from the bend does not change its orientation, all the experimental pressure coefficients still collapse onto a unified distribution. The

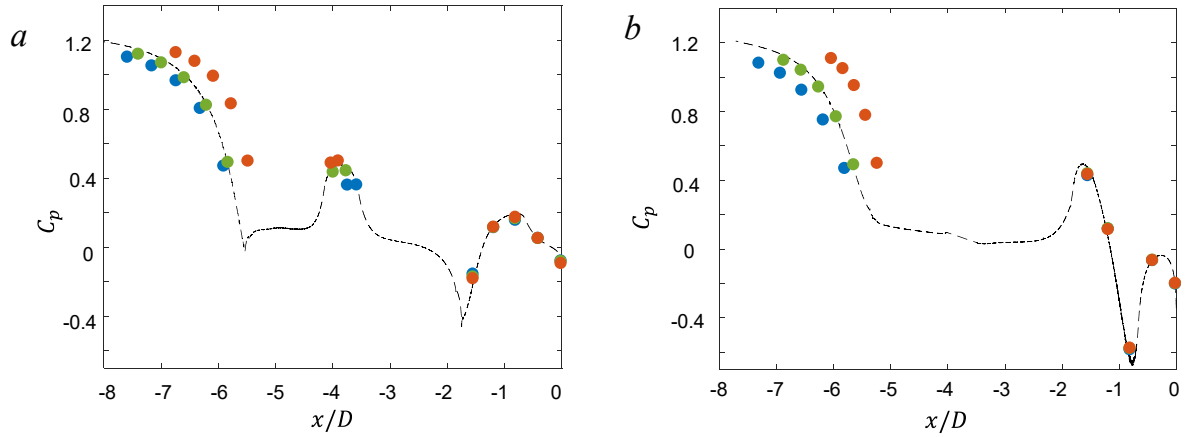

Figure 10. *Measured static distributions of static surface pressure along the bottom (a) and side (b) walls at $M_{AIP} = 0.4$ and $\theta = 20°$(●), $40°$(●), and $60°$(●). The numerical simulations (---) are shown at $\theta = 40°$.*

full pressure distributions along the two central sides of the geometry are extracted from numerical simulations for the fixed $\theta = 40°$. The connection to the internal flow based on these distributions was discussed in connection with Figure 8. Here, reasonable agreement between experimental and numerical results is seen for the simulated $M_{AIP} = 0.4$ flow at $\theta = 40°$. It is noted that even the two isolated measured points about the outer bend apex align just on either side of the numerical local pressure peak about the outer bend.

As a summary of the dependence of the AIP flow on the bend angle θ, Figure 11 shows the measured evolution of the total pressure recovery and distortion for each of the bend angles $\theta = 20°$, 40°, and 60°, over a full range of the Mach numbers $0.1 < M_{AIP} < 0.54$. In addition, equivalent numerical results for $M_{AIP} = 0.4$ are also shown for comparison. Pressure recovery (Figure 11a) depicts a typical drop in recovery with increasing Mach number, leading to just about 2.5% loss at $M_{AIP} = 0.5$. There is a weak dependence on θ at lower Mach numbers, where recovery decreases with θ, but the recovery curves diverge with M_{AIP}, leading to somewhat higher differences at the highest Mach numbers. Numerical results (red symbols) indicate the same trend of decreasing recovery with θ, although all three data points appear slightly offset to higher recoveries compared to experimental curves. Still, the difference is only about 0.2 – 0.3%. As already suggested by the total pressure distributions at the AIP shown in Figure 9, circumferential average distortion descriptor $DPCP_{avg}$ slightly decreases with increasing θ, although the noted differences were rather small. The experimental $DPCP_{avg}$ dependence on θ over the full range of Mach numbers is shown in Figure 11b, where a similar bias towards lower distortion parameters is seen with increasing M_{AIP}, exhibiting some divergence towards higher M_{AIP}, just as in the recovery distributions (Figure 11a). Better numerical prediction is noted with increasing θ, resulting in only 3.5% difference for $\theta = 60°$. Overall, a typical sharp increase in $DPCP_{avg}$ with Mach number is seen in Figure 11b for all the cases shown, where the peak distortion coefficient reaches about $DPCP_{avg} = 0.03$ at $M_{AIP} = 0.5$ for the 40° case.

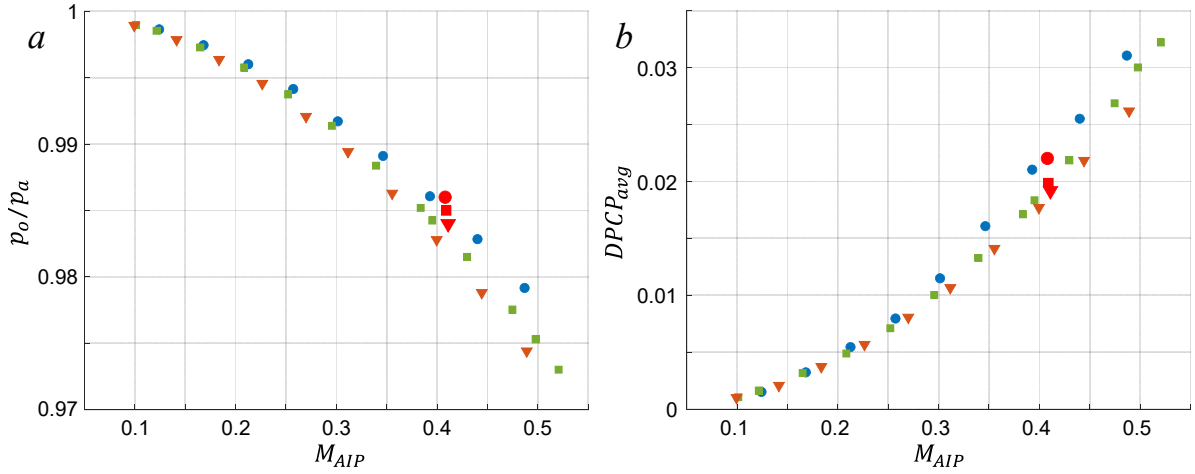

Figure 11. *Experimental total pressure recovery (a) and circumferential averaged distortion (b) with the AIP Mach number for $\theta = 20°$ (■), 40° (▼), and 60° (◆) and the numerical results (red).*

VI. Analysis of the Flow Field

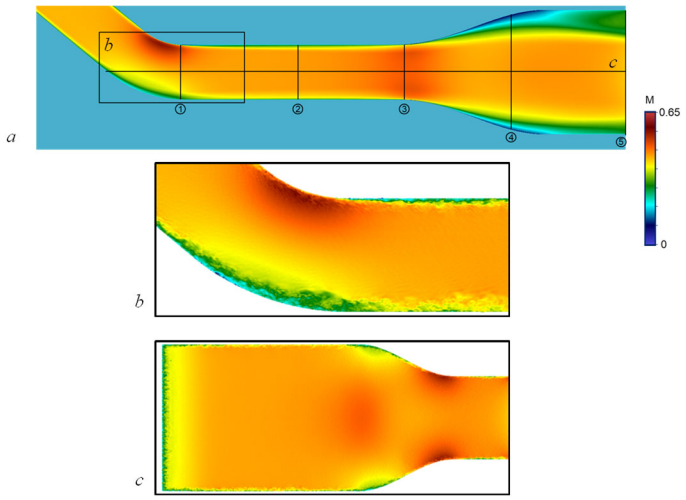

Figure 12. *Color raster plots of distributions of the time-averaged Mach number along the duct centerline (a), instantaneous Mach number at the bend (b), and instantaneous Mach number in a planar slice (c).*

An illustration of the flow field, from the numerical simulations, is shown in Figure 12 for $M = 0.4$ and $\theta = 40°$. Figure 12a shows a centerline slice of Mach number from just upstream of the bend to the AIP. The flow at the bend, highlighted in Figure 12b, shows a low velocity region at the top and bottom surfaces of the duct for this configuration, resulting in a thickening of the boundary layer. The flow continues downstream in the straight rectangular duct section before transition to a circular AIP. This transition consists of the sides of the duct contracting while the top and bottom sides expand. This transition section results in separation on the top and bottom walls. Figure 12c highlights the flow in a planar slice along the center of the duct showing the low and high-speed regions on the side walls that was seen in the pressure plot in Figure 10.

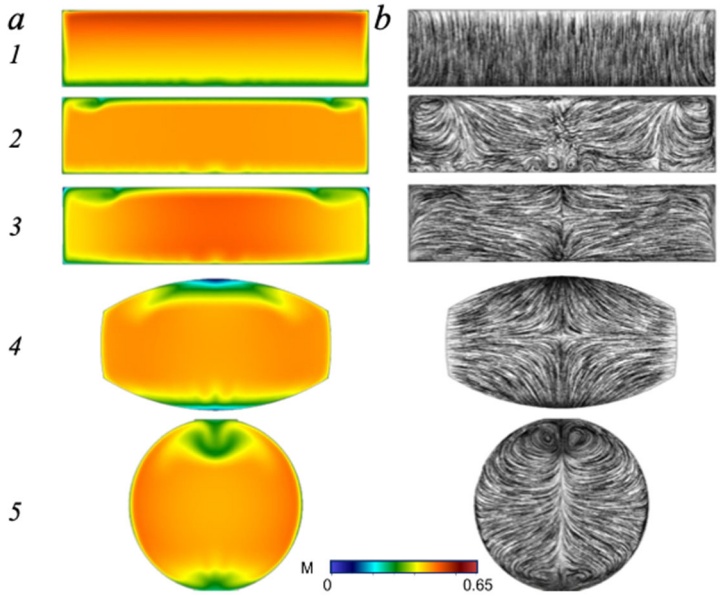

Figure 13. *Cross section slices at locations described in Figure 12 for the time averaged M (a), and corresponding streamlines (b).*

Cross-sections along the diffuser, labeled 1-5 based on Figure 12, are shown in Figure 13a and Figure 13b for Mach number, and tangential streamlines, respectively. The Mach number highlights a low-speed flow region originating from the side walls of the bend in slice-1, which grows inward and larger at the end of the straight rectangular duct in slice 3. As the flow progresses through the transition towards the AIP (slice-5) that flow structure stays intact. Likewise, Figure13b, shows the flattened vortical flow at the wall in slice-1 that moves towards the top wall and becomes rounder as the flow approaches the middle of the straight duct in slice-2. The contraction and expansion of the flow is seen in slice-4, as the geometry transitions from

rectangular-to-circular, before forming characteristic counter-rotating vortices at the top and bottom of the AIP.

The time-averaged turbulent kinetic energy and the streamwise component of the vorticity, at the cross-sections labeled in Figure 12, are shown in Figures 14a and 14b, respectively. The streamwise vorticity aligns well with what was seen in the previous Figures, where high levels of vorticity originate at the side walls of the bend, rolling up towards the top wall and weakening as it moves downstream, seen in slice-3. The vorticity also highlights the counter-rotating vortex pair at the AIP. The turbulent kinetic energy indicates areas in the flow where turbulent fluctuations are highest. Notably, this occurs in the vortical flow originating from the bend, and is carried through the transition section, seen in slice-4, and into the AIP, seen as the outer green lobes in slice-5. At the AIP the highest *TKE* occurs at the top center where the counter-rotating vortices are interacting. While the transition section from rectangular to circular cross-section in this configuration is quite aggressive, inducing its own separation and vorticity, it is clear that the energy from the bend persists through this section and is still felt at the AIP.

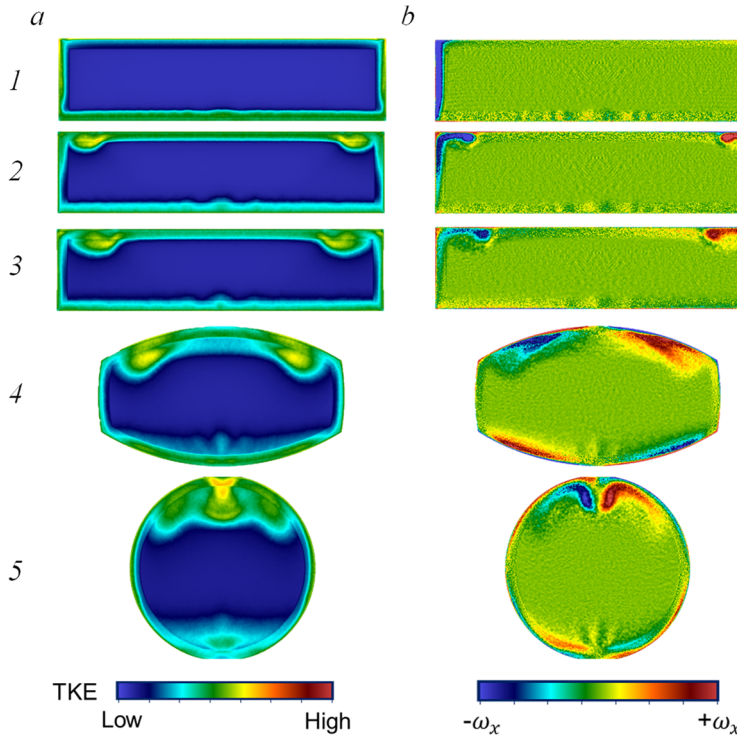

Figure 14. *Cross section slices at the locations described in Figure 12 for the time-averaged turbulent kinetic energy (a), and streamwise vorticity (b).*

To gain a better understanding of how the bend angle affects the flow structure, the turbulent kinetic energy and streamwise vorticity at the AIP are plotted in Figure 15 for $\theta = 20^o$, 40^o, and 60^o. At $\theta = 20^o$ the vorticity induced at the bend is the weakest of the three angles studied, which results in less vortical flow penetration into the middle of the top wall. Therefore, as the flow transitions to the rectangular to circular cross-section at the AIP, this vorticity component remains attached to the wall at the outer left and right sides, seen in Figure 15d. Note, that there are two sources of vorticity at the AIP, the counter-rotating pair as a result of the transition itself, and this vorticity from the bend. As the angle increases, this vorticity component from the bend moves further towards the middle of the duct, resulting in a clear separation from the wall over the top half of the duct at $\theta = 60^o$, seen in Figure 15f. Additionally, at larger duct angles, the vorticity on the bottom half of the duct tends to be suppressed; this showed up in the pressure recovery contours, in Figure 9, as a smaller pressure deficit. The influence of the bend is seen more readily in the turbulent kinetic energy contours, where the larger bend induces stronger vorticity and more energy that persists to the AIP, seen in Figure 15c.

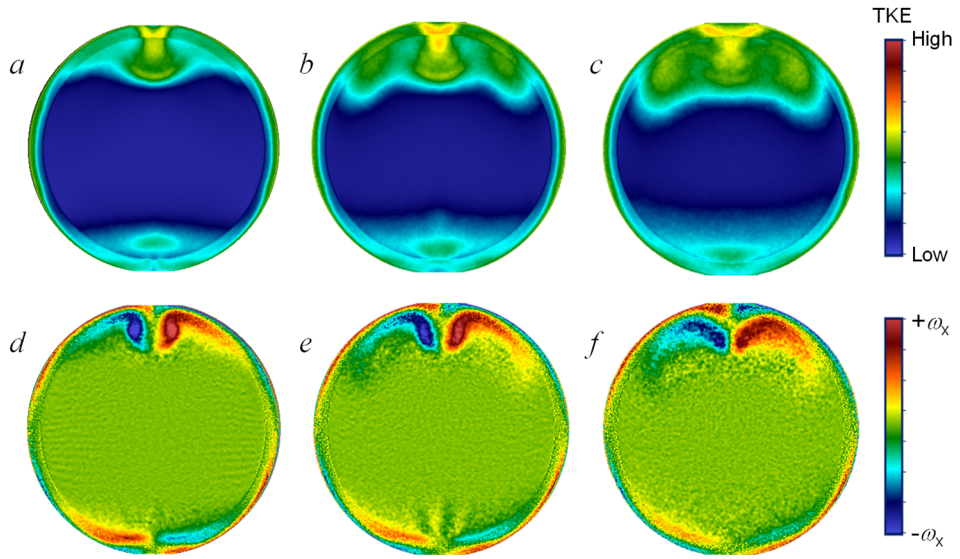

Figure 15. *Turbulent kinetic energy (a, b, c) and streamwise vorticity (d, e, f) for θ = 20° (a ,d), 40° (b, e), and 60° (c, f).*

As was shown, the largest impact on the flow at the AIP for this configuration is the vorticity generated at the side walls at the bend that persist and evolve downstream along the top wall. This evolution can be seen for $\theta = 20^{o}$, 40^{o}, and 60^{o} in the streamlines and wall shear stress along the top wall in Figure 16. The white line in this Figure highlights the location where the bend ends and the straight section begins, the same location as slice-1 in Figure 12a. Figure 16a-c highlights the trend in vorticity that was highlighted in the previous Figures, where the vortical flow regions move towards the center as the duct as the angle increases, and at $\theta = 20^{o}$, this region tends to remain near the top corners. The shear stress, in Figure 16d-f, highlights several important features. First, the shear stress is highest at the bend where the flow accelerates, and it is at this point where the vorticity originates, seen most clearly in Figure 16f. Second, there is a low-speed region downstream of the bend, seen as the dark blue just behind the white line, where the boundary layer is thickening that grows as the angle increases. Third, there is an interaction between these two regions, seen as the light-blue to dark-blue transition along the length of the

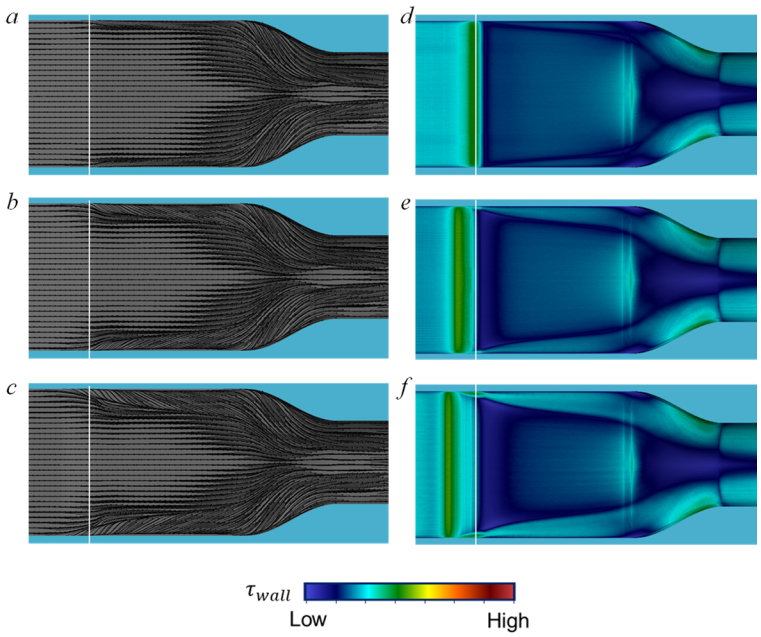

Figure 16. *Numerical surface streamlines and wall shear stress for θ = 20° (a, d), 40° (b, e), and 60° (c, f). A white line indicates the end of the bend.*

duct, suggesting a non-uniform boundary layer profile along the cross-section. This could also be seen in the Mach number contour in slice-2 and slice-3 in Figure 13a.

VII. Conclusions

The flow within a new reconfigurable diffuser design testbed coupling integrated AFC technologies with numerical design tools to enable adaptive, rapid variations of desired design characteristics was assessed using experimental measurements and simulations. The diffuser testbed provides variable mass flow rate up to AIP Mach number of 0.7 while the adaptive design enables sectional changes that provide variations in the test section aspect ratio, bend angle, and bend radius. The present investigations considered experimental and numerical assessment of the effects of the diffuser's bend angle θ (20°, 40°, and 60°) on the internal flow at aspect ratio $AR = 4$ and the bend radius $r_b = 0.5D_{AIP}$, the diameter of the aerodynamic interface plane. The experimental measurements were guided by and compared with the numerical simulations that provided additional details of the flow evolution within the diffuser testbed.

Prior to the main study, a procedure for calibration of the mass flow rate through the diffuser using the bellmouth section was developed in a simplified duct having a circular cross section and nominally uniform flow through the AIP. The mass flow rate was computed using the measurements of a 40-probe total pressure rake at the AIP, in conjunction with an azimuthal array of static pressure ports and was in excellent agreement with the numerical simulations. These measurements were used for calibration against the measured pressure drop across the inlet bellmouth to avoid inaccuracies when the AIP flow is not uniform.

It is shown that within the present range of bend angles the flow downstream of the bend becomes dominated by the evolution and downstream growth of corner streamwise vortices. While the vorticity concentrations over the concave (outer) surface of the bend become flattened at the AIP ostensibly owing to the radial pressure gradient, the vortices formed along the convex (inner) surface of the bend spread radially towards its center and evolve into a counter rotating dominant vortex pair at the AIP. It was also shown that while the boundary layers over the curved surfaces of the bend become thicker as its angle increases, at this bend radius ($0.5D_{AIP}$) the flow does not separate on either curved surface. As a result, the losses in total pressure that are strongly dependent on Mach number and weakly dependent on θ do not exceed about 2.5% at $M_{AIP} = 0.5$. The characteristic measure of the total pressure distortion, the circumferential average distortion parameter, appears to decrease slightly with θ, decreasing 15% from θ=20° to θ=60° at M_{AIP} = 0.5Following the preliminary assessment of the internal flow, active flow control will be implemented and assessed in experiments and CFD using internal arrays of fluidically oscillating jets.

Acknowledgment/Disclaimer

This work was sponsored by the Office of Naval Research (ONR), under grant number N000142312500. The views and conclusions contained herein are those of the authors only and should not be interpreted as representing those of ONR, the U.S. Navy, or the U.S. Government. The authors acknowledge the computational resources provided by the Department of Defense (DoD) High Performance Computing Modernization Program, specifically the DoD Air Force Research Laboratory and Navy DoD Supercomputing Resource Center systems.

References

Amitay, M., Pitt, D., and Glezer, A. "Separation control in duct flows," *Journal of Aircraft* Vol. 39, No. 4, 2002, pp. 616-620.

Anderson, B. H., Miller, D. N., Addington, G. A., and Agrell, J. "Optimal Micro- Jet Flow Control for Compact Air Vehicle Inlets." NASA Glenn Research Center, 2004.

Anderson, B.H., Gibb, J., "Study on Vortex Generator Flow Control for the Management of Inlet Distortion," *J. Prop. Pow.* **9**, pp. 422-430, 1993.

Bres, G. A., Bose, S. T., Emory, M., Ham, F. E., Schmidt, O. T., Rigas, G., and Colonius, T., "Large-Eddy Simulations of Co-annular Turbulent Jet Using a Voronoi-Based Mesh Generation Framework." AIAA Paper 2018-3302, 2017.

Burrows, T. J., Vukasinovic, B., Lakebrink, M. T., Mani, M., and Glezer, A. "Control of flow distortion in offset diffusers using trapped vorticity," *International Journal of Heat and Fluid Flow* Vol. 75, 2019, pp. 122-134.

Burrows, T.J., Vukasinovic, B., Glezer, A., Lakebrink, M.T., and Mani, M., "Experimental and Numerical Investigation of Active Flow Control of a Serpentine Diffuser," *AIAA J.* **59**, pp. 607-620, 2021.

Burrows, T.J., Vukasinovic, B., Glezer, A., Lakebrink, M.T., and Mani, M., "Controlled Flow in a Serpentine Diffuser with a Cowl Inlet," *J. Aircraft*, published online, 2024. https://doi.org/10.2514/1.C037992

Garnier, E. "Flow Control by Pulsed Jet in a Curved S-Duct: A Spectral Analysis," *AIAA Journal* Vol. 53, No. 10, 2015, pp. 2813-2827.

Gartner, J., and Amitay, M. "Flow Control in a Diffuser at Transonic Conditions," *45th AIAA Fluid Dynamics Conference*. American Institute of Aeronautics and Astronautics, 2015-2484.

Germano, M., Piomelli, U., Moin, P., & Cabot, W. H. "A Dynamic Subgrid-Scale Eddy Viscosity Model". *Physics of Fluids A - Fluid Dynamics*, *3*, 1991, pp. 1760–1765.

Gissen, A. N., Vukasinovic, B., McMillan, M. L., and Glezer, A. "Distortion Management in a Boundary Layer Ingestion Inlet Diffuser Using Hybrid Flow Control," *Journal of Propulsion and Power* Vol. 30, No. 3, 2014, pp. 834-844.

Hall, G., Hurwitz, W., Tiebens, G., Norby, W., Singshinsuk, P. and Wilt, C., "Development of the F/A-18 E/F air induction system," *AIAA Paper* 93-2152, 1993.

Ham, F., Mattsson, K., and Iaccarino, G., "Accurate and Stable Finite Volume Operators for Unstructured Flow Solvers," CTR Annual Research Briefs, 2006, pp. 243–261.

Harrison, N., Anderson, J., Fleming, J., and Ng, W. "Active Flow Control of a Boundary Layer-Ingesting Serpentine Inlet Diffuser," *Journal of Aircraft* Vol. 50, No. 1, 2013, pp. 262-271.

Kawai, S., and Larsson, J., "Wall-Modeling in Large-Eddy Simulation: Length Scales, Grid Resolution, and Accuracy," CTR Annual Research Briefs, 2010, pp. 39–46. https://doi.org/10.1063/1.3678331.

Mathis, R., Duke, D., Kitsios, V., and Soria, J. "Use of zero-net-mass-flow for separation control

in diffusing S-duct," *Experimental Thermal and Fluid Science* Vol. 33, No. 1, 2008, pp. 169-172.

Owens, L.R., Allan, B.G., Gorton, S.A.,"Boundary-Layer-Ingesting Inlet Flow Control," *J. Aircraft.* **45**, pp. 1431-1440, 2008.

Rabe, A. "Effectiveness of a serpentine inlet duct flow control scheme at design and off- design simulated flight conditions." ProQuest Dissertations Publishing, 2003.

Scribben, A., Ng, W., and Burdisso, R. "Effectiveness of a Serpentine Inlet Duct Flow Control Technique at Design and Off- Design Simulated Flight Conditions," *Journal of Turbomachinery* Vol. 128, No. 2, 2006, pp. 332-339.

Society of Automotive Engineers Inc., "Gas Turbine Engine Inlet Flow Distortion Guidelines," ARP 1420 Rev. C, 2017.

Tanguy, G., MacManus, D. G., Zachos, P., Gil-Prieto, D., and Garnier, E., "Passive Flow Control Study in an S-Duct Using Stereo Particle Image Velocimetry," *AIAA J.* **55**, No. 6, pp. 1862-1877, 2017.

Vreman, A. W., "An Eddy-Viscosity Subgrid-Scale Model for Turbulent Shear Flow: Algebraic Theory and Applications," Physics of Fluids, Vol. 16, No. 10, 2004, p. 3670.